

# A Novel Design Technique of Hypersonic Gliding Vehicle

Tian-tian ZHANG\*, Wei HUANG\*, Shi-bin LI\*, Zhen-guo WANG\*

\* Science and Technology on Scramjet Laboratory

National University of Defense Technology, Changsha 410073, China

## Abstract

Hypersonic gliding vehicle is attracting an increasing attention because of its high lift-to-drag ratio and high cruising speed. Based on the design theory of cone-derived waverider, this paper proposes a novel design approach of hypersonic gliding vehicle, which is accommodated in a wide speed range. The parametric method employed in ascender line makes it possible to control the overall configuration. Numerical analysis demonstrates that this kind of aircrafts own good wave-ride properties in the designed speed range. The simplified trajectory performance analysis shows a wavy trajectory with long range, which makes it suitable for long-distance transportation and tactical defense penetration.

## 1. Introduction

Nowadays, interplanetary travel and reusable vehicle are attracting an increasing attention in aerospace field. Vehicles traveling from earth into space have to overcome various difficulties. For example, robust aerodynamic properties are required in different altitudes and different velocities. Being a kind of vehicle with high speed and stable gliding property, which is more comfortable for passengers than the ballistic vehicles, Hypersonic Gliding Vehicle (HGV) has a promising prospect in space travel. The aerodynamic design of HGV is of great importance because a good configuration would take full advantage of the atmosphere to increase lift and reduce drag thus transporting more payloads with fewer fuel cost.

Traveling in supersonic and hypersonic conditions, waverider's whole lower surface is enclosed in a designed shock wave. As a result, relatively high lift to drag ratio will appear in a given attack angle. Küchemann firstly proposed the design technique of waverider and analyzed the characteristics of this kind of vehicle [1]. Following researches have been done after this innovation. Ding et al investigated the influence of the surface pressure distribution of a basic flow field on the shapes and performances of waveriders [2]. They found that changing in base flow's surface pressure distribution will permit greater flexibility for waverider design and optimization. Chen et al investigated the performance of waveriders with blunted edges [3]. They indicated that waveriders are unpractical in real flight because the sharp edge will cause great challenge to thermal protection system. However bluntness of the edge will severely decrease waveriders' aerodynamic performance. Liu et al did numerous experiments and CFD works to study the aero-heating characteristics of blunted waverider [4, 5]. The results in their works are worth referring in waverider study. Lobbia also experimentally investigated the waverider, which is designed using computational fluid dynamics, in the speed of Mach 5 [6]. The schlieren and oil-flow visualization results showed the attached shock-wave characteristics and reproduction of the conical generating flow field by the waverider at on-design conditions.

However, been designed under a given Mach number, waverider as well as other traditional hypersonic vehicles is not proved to own good performance under other Mach number conditions. A vehicle designed considering a wide speed range is urgent for future application.

## 2. Wide-speed-range HGV design approach

Before introducing the novel design approach of wide-speed-range HGV, the cone flow theory in hypersonic environment and the design technique of waverider will be briefly reviewed.

Waveriders are normally designed using the inverse design philosophy [7]. Firstly, the flow structure of free flow passing a cone, which can be treated as the expected flow field, will be certain as long as the Mach number is given. This flow field will span all the flow characteristics generated by the target waverider. Secondly, the designer defines the pattern of the upper-surface base curve (UBC). Waverider's leading edge is obtained by tracing the streamlines from UBC upstream in the free flow field until the shock wave is intersected. The streamlines between UBC and the leading edge compose waverider's upper surface. Lastly, based on the generated flow field, the lower surface will be obtained by tracing from the leading edge to the base plane along the cone flow stream direction. In comparison with

two-dimensional (wedge) flow fields, conical generating flowfields offer the possibility of higher volume designs [6]. Numerical method based on Taylor-Maccoll equation, which is listed as follow, is proved to be efficient to analyze the supersonic conical flow.

$$\frac{\gamma-1}{2} \left[ V_{\max}^2 - V_r^2 - \left( \frac{dV_r}{d\theta} \right)^2 \right] \left[ 2V_r + \frac{dV_r}{d\theta} \cot \theta + \frac{d^2V_r}{d\theta^2} \right] - \frac{dV_r}{d\theta} \left[ V_r \frac{dV_r}{d\theta} + \frac{dV_r}{d\theta} \left( \frac{d^2V_r}{d\theta^2} \right) \right] = 0 \quad (1)$$

There is no closed-form solution to this equation and it must be solved numerically. Readers can refer to Anderson's monograph to find its meaning and numerical procedure solving this equation [8].

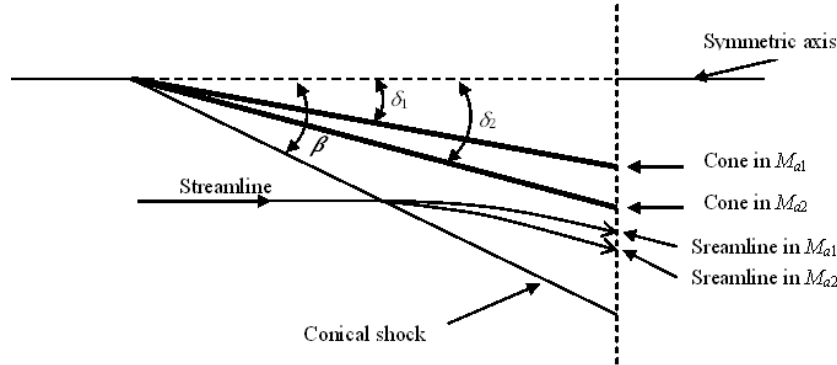


Figure 1: Comparison of equal-shock-angle flow in different Mach numbers.

The design of a wide-speed-range HGV is based on the design philosophy of waverider. When the conical shock wave is fixed, the base cone as well as the conical flow differs with the changing of Mach number. As shown in Figure 1, the conical shock is fixed with the angle of  $\beta$ . In this figure, assuming that  $Ma_1 < Ma_2$ , thus the cones' angles have the following relation,  $\delta_1 < \delta_2$ . A typical streamline in the free stream change its direction after passing the conical shock. By solving Eq. (1) we may find that the streamline behind the shock in  $Ma_1$  will be closer to the symmetric axis than the streamline in  $Ma_2$ . As a result, the corresponding waverider will show the property that the higher the Mach number is, the thicker the waverider will be.

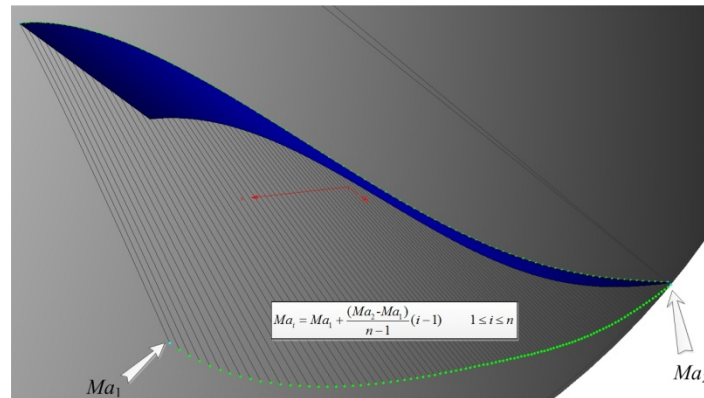


Figure 2: The design schematic of wide-speed-range vehicle.

From the analysis above, it is obvious that when the conical shock is fixed, the design of UBC will determine the shape of the upper surface as well as the leading edge. As can be seen in Figure 2, the half of the vehicle is considered. The design of the UBC determines the shape of the upper surface. The upper surface interacts with the conical shock forming the vehicle's leading edge. The leading edge can be divided into points and streamline-tracing technique will be applied from each point according to different Mach number. When the design Mach

number on the symmetric plane is  $Ma_1$  and the Mach number on the trailing margin is  $Ma_2$ , the Mach number in between can be determined according to arithmetic progression.

$$Ma_i = Ma_1 + \frac{(Ma_2 - Ma_1)}{n-1}(i-1) \quad 1 \leq i \leq n \quad (2)$$

With streamlines tracing from different points on the leading edge according to different Mach number, the lower surface can be acquired by lofting method based on the streamlines. Finally, a wide-speed-range HGV will be generated and it is expected to have excellent aerodynamic performance in the Mach number between  $Ma_1$  and  $Ma_2$ .

### 3. Parametric method

From the design technique we know that the configuration of a certain wide-speed-range HGV is mainly affected by the generating flow field and the shape of UBC. Considering a cone with non-dimensional unit length traveling in the flow with Mach number from  $Ma_1$  to  $Ma_2$ , the shock angle  $\beta$  will determine the flow characteristic. The UBC can be expressed by a function, which consists of all the parameters affecting its shape. To frame the UBC function in Cartesian coordinate, the origin is located on the cone's vertex with the  $Z$  axis points to the direction of the cone's bottom and  $Y$  axis points upward. The direction of  $X$  axis can be derived by the right hand spiral theorem. The coordinates of the two ends, namely  $(\pm x_{sb}, y_{sb}, 1)$ , are efficient to specify the vehicle's width. They can be fixed if the dihedral angle between the vertical plane and the plane constructed by one of the ends and the cone's center shaft is given. The dihedral angle can be presented by  $\varphi$ . Therefore, the two coordinates are:

$$(\pm x_{sb}, y_{sb}, 1) = (\pm \tan \beta \sin \varphi, \tan \beta \cos \varphi, 1) \quad (3)$$

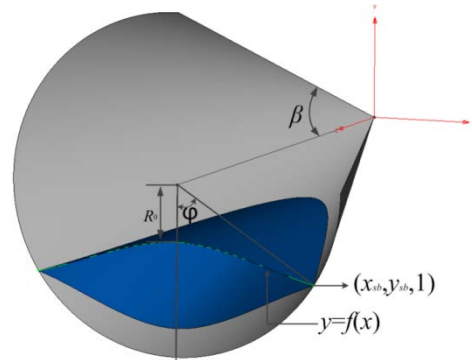


Figure 3: Parametric method of wide-speed-range vehicle

The position of the summit of the UBC can be specified by the distance with the center shaft, namely  $R_0$ . Furthermore, the ratio  $S$  between  $R_0$  and the radius of the cone's bottom is normally used to replace  $R_0$ .

$$R_0 = S \cdot \tan \beta \quad (4)$$

Three points on the UBC has been fixed, thus the symmetric function can be parameterized as follow:

$$y = y_{sb} + A(x^2 - x_{sb}^2)^p$$

$$A = (-1)^{p+1} \frac{(y_{sb} - R_0)}{x_{sb}^{2p}} \quad (5)$$

It is clear that another parameter  $p$  should be designed to determine the formula's order.

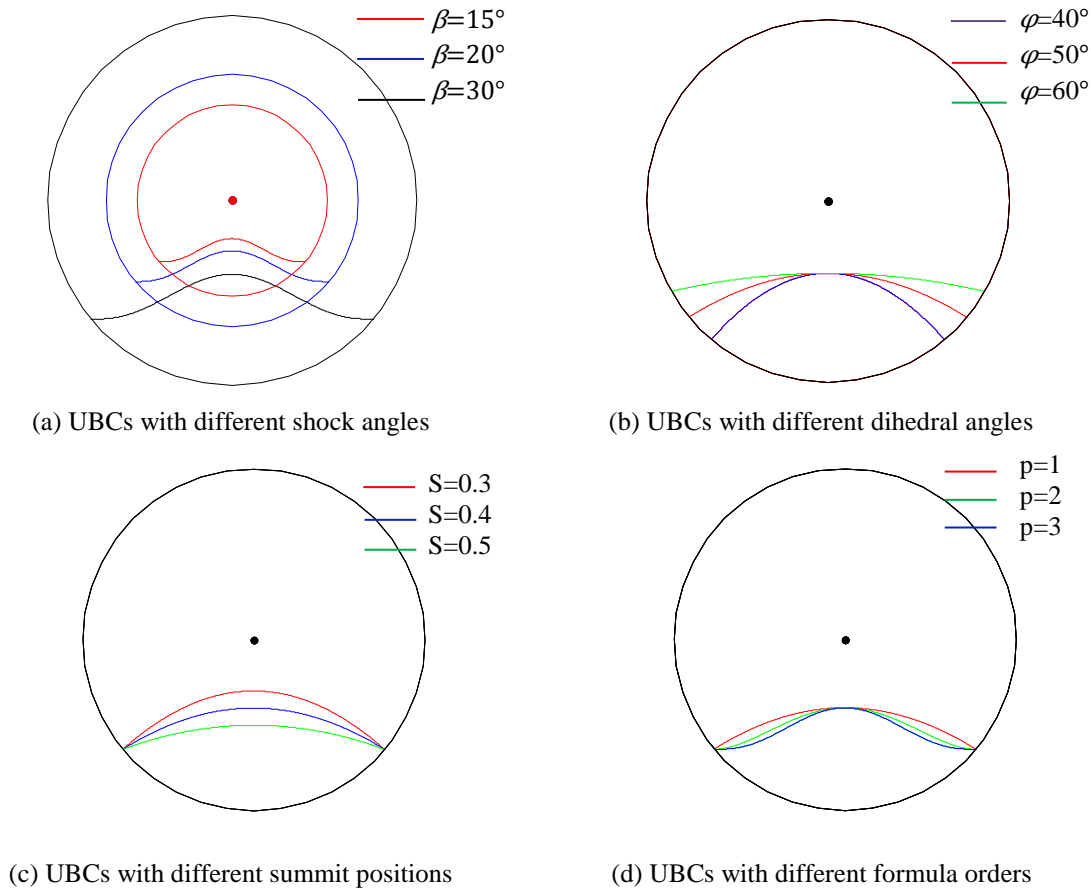


Figure 4: The influence of different parameters on the UBC's shape

Figure 4 presented the influence of the 4 parameters on the UBC's shape respectively. Figure 4(a) shows that  $\beta$  changes the radius of the cone's bottom circle, thus affects UBC's position and size. Figure 4(b) tells that the dihedral angle changes the position of the interaction points between UBC and the base circle, thus changes UBC's curvature. Figure 4(c) shows that  $S$  changes the position of UBC's vertex. Since the positions of the two ends are fixed, the curvature seems to change along with  $S$ . Lastly, figure 4(d) shows the characteristics of polynomials with different orders.

After the determination of UBC's shape, every coordinate on UBC corresponds to certain point on the leading edge. That is:

$$(x, y, 1) \rightarrow (x, y, \frac{\sqrt{x^2 + y^2}}{\tan \beta}) \quad (6)$$

Therefore, the leading edge can be obtained by connecting all the points mapping from UBC. Giving every point on the leading edge a certain Mach number and tracing the homologous streamlines, the lower surface of a wide-speed-range HGV will be generated.

#### 4. Numerical analysis

Figure 5 presents a typical wide-speed-range HGV generated by the approach introduced in last section. In this sample, the shock angle is set to  $20^\circ$  and the cone's length is 1. The dihedral angle is  $40^\circ$ , while the ratio  $S$  is set to 0.4. The UBC of this vehicle is a polynomial curve with the order  $2p=4$ , which can refer to Eq. (5). The design Mach number is 6 to 12 from the edge to the vehicle's symmetric plane continuously.

In this section, vehicles with different design Mach number are compared by numerical method. The UBC of these vehicles are the same with the expression of  $y=1.7233x^2 + 0.096$ . The characteristics of these vehicles are listed in Table 1. Case1 and Case2 are waveriders with the design Mach number of 10 and 6 respectively. Case3 and Case4 are two wide-speed-range HGVs with different changing directions of Mach number.

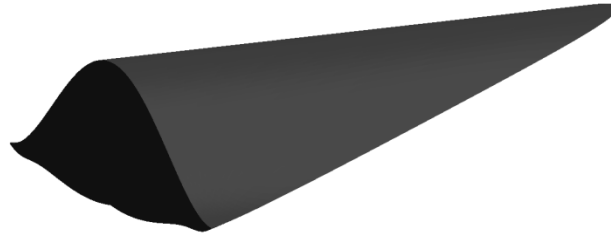


Figure 5: A typical wide-speed-range HGV

Table 1 Characteristics of four configurations

Configurations	Characteristics
<b>Case1</b>	Waverider designed under Ma=10.
<b>Case2</b>	Waverider designed under Ma=6.
<b>Case3</b>	Wide-speed-range HGV designed with Mach number of 10 to 6 from the edge to the vehicle's symmetric plane continuously.
<b>Case4</b>	Wide-speed-range HGV designed with Mach number of 6 to 10 from the edge to the vehicle's symmetric plane continuously.

CFD simulation has been carried out based on the four configurations. In order to obtain high-fidelity aerodynamic result, structural grids are generated around the body by commercial software POINTWISE (Version V17.2R1) as shown in Figure 6. The grid has been refined to the direction of the vehicle with the grid height of the first layer  $\Delta s=0.01$  mm to confirm  $Y_{plus} y^+ < 5$ , so that the result around it can be more precise. The shock wave position is predicted according to the design approach thus the grid is also refined toward the predicted shock wave so that it can be catch more clearly. The total number of the grid cells is 1133200.

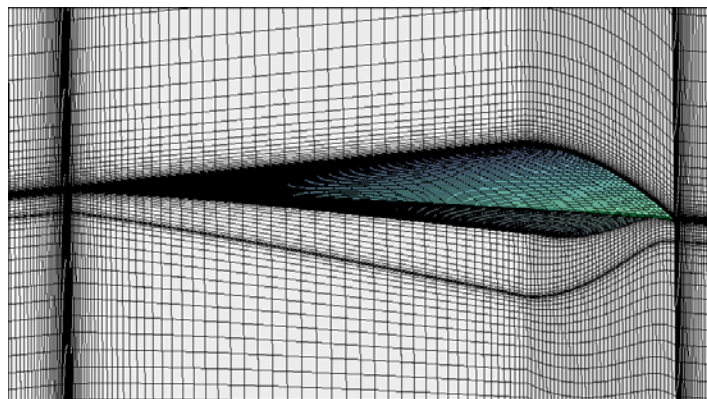


Figure 6: Schematic diagram of the structured grid employed on Case4

Air property at the altitude of 25 kilometers is utilized with the static pressure of 2549.22Pa and the static temperature of 221.552K. The three-dimensional implicit equations and the density based inviscid model have been employed to simulate the flow field around the configuration using the commercial software FLUENT (Version 6.3.26). The flow is treated as ideal gas with the Mach number of 6, 8 and 10 respectively, which means in the two ends and the middle place of the design Mach number.

The inviscid pressure contours at the base planes of Case1 in the flow of  $Ma=10$  (left) and Case2 in the flow of  $Ma=6$  (right) are shown in Figure 7, respectively. Since both the configurations share the same UBC, the leading edge will also be the same. It shows good wave-ride performance of both the waveriders in corresponding design Mach numbers. What's more, the CFD result shows consolidated cone shock of two cases, which agreed well with the equal-shock-wave design principle. As a result, we can summarize that the waveriders designed using stream-tracing method can satisfy the requirement of wave-ride performance and the lower surfaces of the configurations are covered in the cone shock.

Figure 8 shows the inviscid pressure contours at the base planes of Case3 and Case2 in the Mach number of 6. Both cases share the same design Mach number in the symmetric planes, namely  $Ma=6$ . The shock wave of both cases should coincide well at this region theoretically and the contours in this figure proved this prediction. However, the overall pressure distribution of both the cases differs a lot. It can be seen that pressure value on the lower surface of Case3 is greater than that on the lower surface of Case2. This is due to the thickness of Case3 overweigh the thickness of Case2 and Case3 derives stronger shock wave, which results in a greater pressure distribution behind the shock.

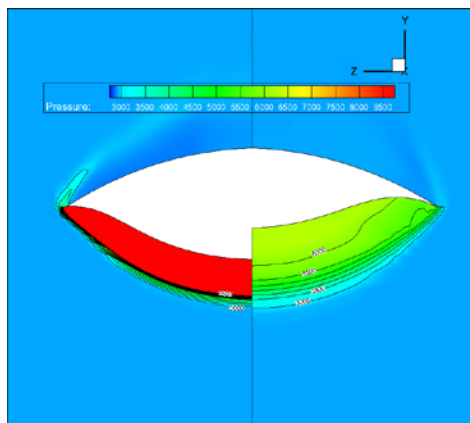


Figure 7 Comparison of pressure contours of Case1 in Ma10 (left) and Case2 in Ma6 (right).

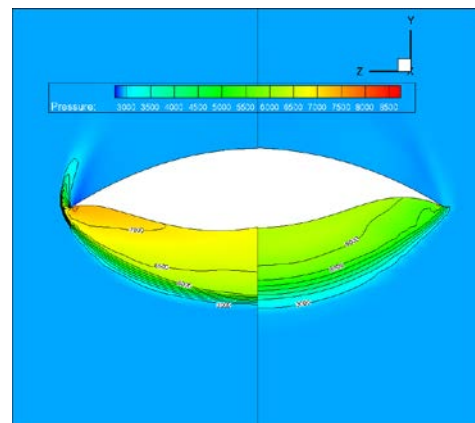


Figure 8 Comparison of pressure contours of Case3 (left) and Case2 (right) in Ma6.

Figure 9 illustrates the inviscid pressure contours at the base planes of these four cases in Mach 10 and Mach 6 respectively. The configuration in Case1 is the waverider designed in Mach 10, thus it perform well in the design Mach number. However, when this configuration is traveling in the flow of Mach 6, the contour in the trailing edge shows the appearance of detached shock wave. The high pressure under the vehicle turns upward to the upper surface thus reduces the lift of the body. By contrast, Case2, which is the waverider designed in Mach 6, reveals expected wave-ride performance in the flow of Mach 6, but when the Mach number of the incoming flow is 10, the shock becomes so body-fitted that it is covered by the under surface. As a result, the undersurface suffers non-uniform pressure with high pressure in the center place and lower pressure in the two sides. This reflects the redundancy in design since the two sides do not have obvious effect. Both of Case3 and Case4 perform well in Mach 10 and show good wave-ride performance. It should be noticed that the lower surface of Case4 suffer more uniform pressure than Case2 although the design close to the configuration's verge is based on lower Mach number. When it goes to Mach 6, Case3 as well as Case4 shows detached shock wave on the two sides, which results in the high pressure transferring from the lower surface to the upper surface. In comparison with Case1, this phenomenon improves a lot.

Figure10 shows the pressure distribution of the flow around Case3 in Mach 10. This figure presents the good wave-ride performance of wide-speed-range HGV in given Mach number. The lower surface owns a homogeneous pressure distribution on it and it is covered by a high pressure environment while the upper surface is surrounded by the free flow condition. Therefore, this kind of configuration owns high lift as well as high lift-to-drag ratio.

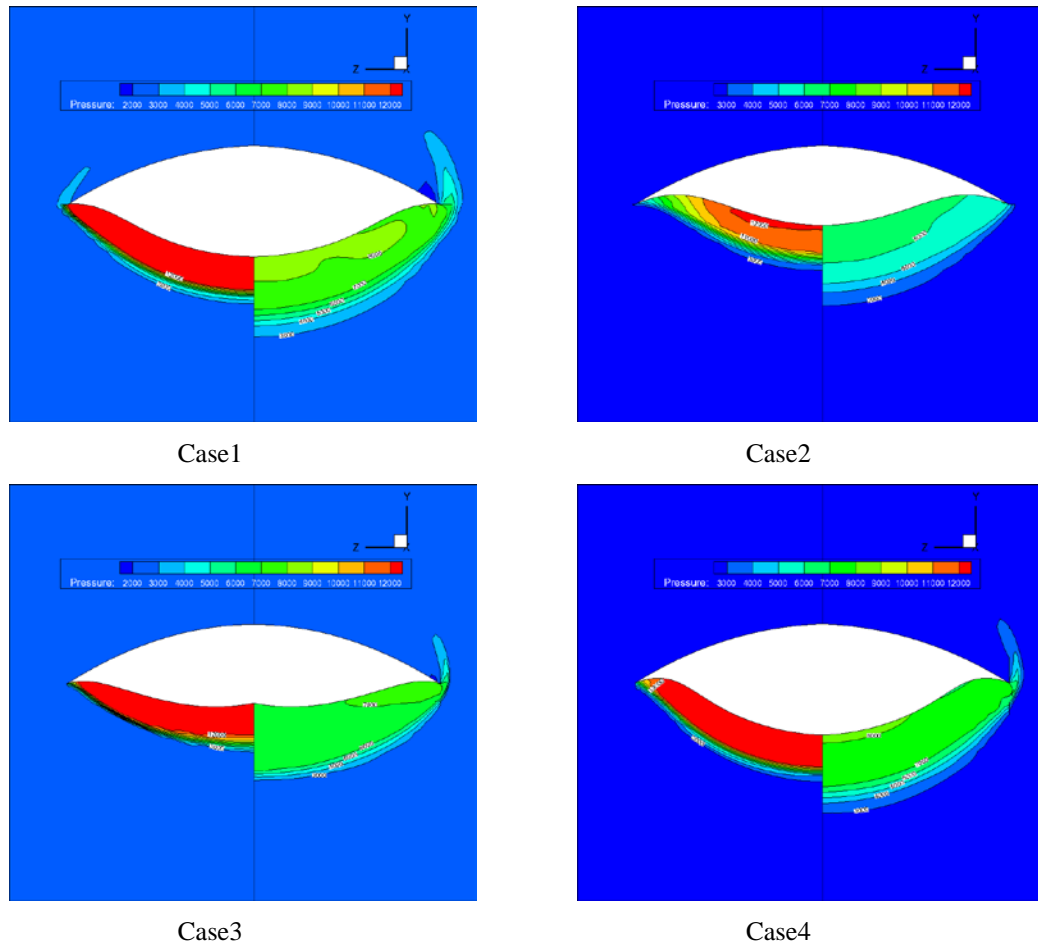


Figure 9: Pressure contours comparison of different configurations in Ma10 (left) and Ma6 (right).

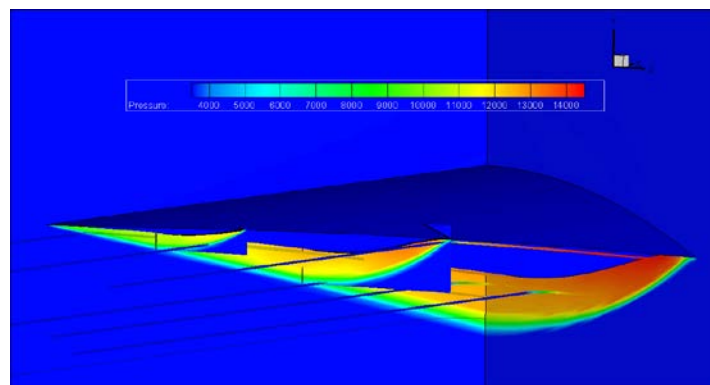


Figure 10: Pressure distribution of the flow around Case3 in Ma10.

The aerodynamic properties of these four configurations are illustrated in Figure 11-Figure 13. The axial force, normal force and the lift-to-drag ratio ascend with the increase of the angle of attack. When the angle of attack is fixed, Case1 owns the greatest value of axial force and normal force while Case2 owns the lowest value. The value of Case3 outweighs the value of Case4. On the contrary, the properties of the lift-to-drag ratio show that Case2 owns the best performance and it follows by Case3, Case4 and Case1 respectively. There has been specialized study on the aerodynamic performance of waveriders with different design Mach number. What we concern in this article is the performance of wide-speed-range HGV. As can be seen in Figure 11-Figure 13, Case3 owns more unique properties than Case 4 and Case4 perform closer to Case1. The axial force, normal force and the lift-to-drag ratio of Case3 are all between those of waveriders designed in lower and higher Mach number. Comparing with Case1, Case3 owns

higher lift-to-drag ratio. Moreover, the minimum value between Mach 6 to 10 of Case3 is also larger than the maximum value of Case1. Comparing with Case2, Case3's body is plumper than Case2. It also has greater value of volumetric ratio. Additionally, Case3's range of lift force is also larger than Case2, which means that when cruise is needed, Case3 is qualified to carry more payloads.

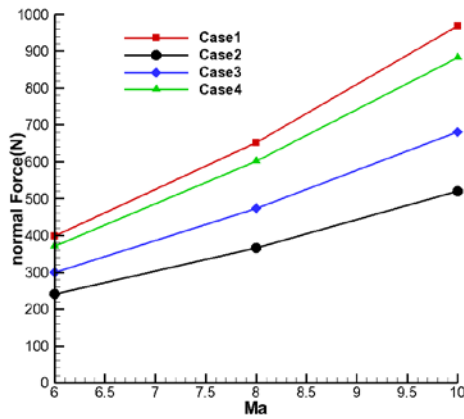


Figure 11: Comparison of normal force of four cases.

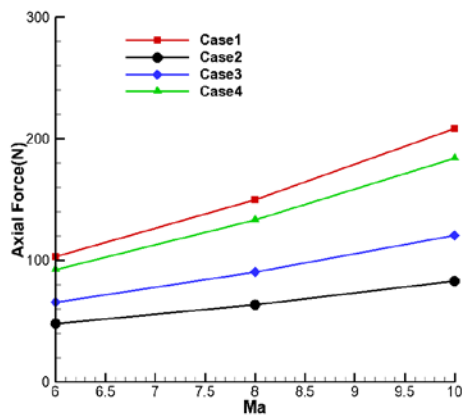


Figure 12: Comparison of axial force of four cases.

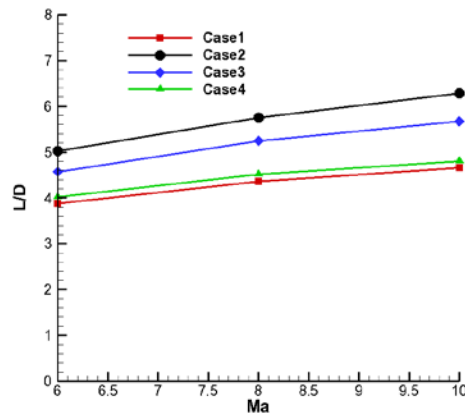


Figure 13: Comparison of lift-to-drag ratio of four cases

In brief, the wide-speed range HGV is a novel design approach for hypersonic gliding vehicle which can travel in a large speed range. Comparing with the waverider designed in a given Mach number, the properties of this type of vehicles are a kind of tradeoff and they can satisfy the engineering requirements likewise. In addition, wide-speed range HGV owns good wave-ride performance in the design speed range and the undersurfaces suffer more uniform pressure, which gives them a bright prospect.

## 5. Trajectory analysis

The re-entry strategy of a gliding vehicle is quite different with traditional ballistic re-entry. Its trajectory is severely affected by aerodynamic performance. This kind of vehicles is suitable to operate three dimensional maneuvering in a wide speed range and wide flying area. These vehicles can change speed and direction by the aid of aerodynamic forces. As a result, the trajectory optimization and control of gliding vehicle have attracted an increasing concern [9-12].

The wide-speed-range vehicle of Case 3 in Table 1 has been studied numerically and the Mach related aerodynamic coefficients, when the angle of attack is 0, have been listed in Table 2. Combining with ballistic equations, the flying trajectory of the HGV in Case 3 can be acquired assuming that the attack angle is 0.

Table 2. Aerodynamic coefficients of wide-speed-range HGV in Case 3

Ma	2	4	6	8	10	15	20
$C_L/10^{-3}$	7.568	5.590	4.630	4.125	3.805	3.360	3.000
$C_D/10^{-3}$	3.443	1.671	1.090	0.859	0.735	0.598	0.550
L/D	2.198	3.345	4.248	4.802	5.175	5.619	5.455

Earth is assumed as a static and homogeneous sphere with parallel gravitational field. Then the re-entry kinematic equations of aircraft without sideslip and rolling motion can be listed as bellow.

$$\frac{dr}{dt} = V \sin \gamma \quad (7)$$

$$\frac{d\beta_e}{dt} = \frac{V \cos \gamma}{r} \quad (8)$$

$$\frac{dV}{dt} = -\frac{\rho S_{ref} C_D V^2}{2m} - g \sin \gamma \quad (9)$$

$$\frac{d\gamma}{dt} = \frac{1}{V} \left[ \frac{\rho S_{ref} C_L V^2}{2m} - \left( g - \frac{V^2}{r} \right) \cos \gamma \right] \quad (10)$$

In the equations above,  $r$ ,  $t$ ,  $V$  and  $m$  represents for geocentric distance, flight time, flight speed and the mass respectively.  $\gamma$  and  $\beta_e$  are the local velocity angle and the range angle.  $\rho$ ,  $g$  and  $S_{ref}$  are the air density, the acceleration of gravity and the reference area respectively. Finally,  $C_L$  and  $C_D$  are the lift coefficient and the drag coefficient, which are calculated by interpolation using the information in Table. 2.

This flight is assumed as a reentry flight from near-earth orbit whose initial velocity is 5000 m/s. The initial re-entry altitude is 90 km and the re-entry angle is  $3^\circ$ . The HGV in Case 3 is 50 kg weight and the reference area is  $1 \text{ m}^2$ . The earth radius is 6371 km and the gravitational constant is  $\mu=3.986 \times 10^5 \text{ km}^3/\text{s}^2$ . The atmospheric parameter adopts standard atmospheric table.

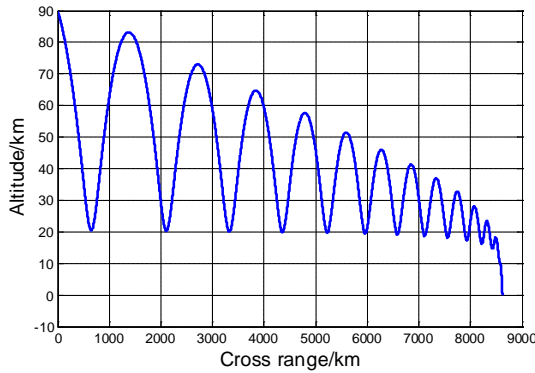


Figure 14: An example of Flight strategy of Case3.

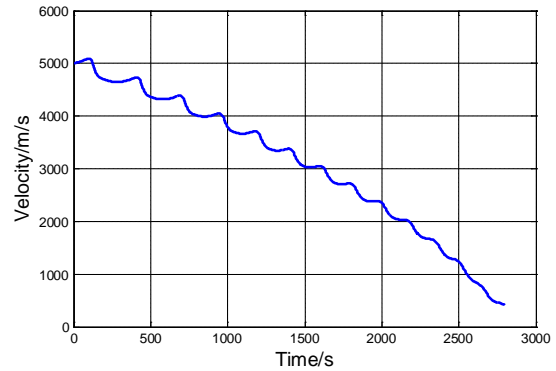


Figure 15: Velocity's property during reentry.

Figure 14 shows the reentry strategy of wide-speed-range HGV in Case 3. It is a typical saltatory ballistic curve and the flight energy decreases with each leap while the leap height decrease simultaneously. The trajectory height remains above 20 km before the cross range reach 6000 km. Not until the range reach 8500 km, the energy becomes too deficient to afford a further leap and it presents a curve of reentry. The total flight range is 8620 km with the total flight time of 209 s.

The reentry velocity curve in Figure 15 shows the decline tendency of velocity value and each leap in the trajectory correspond with a stage of velocity decrease. This is caused by the friction and heating of the air that convert kinetic energy into other forms of energy. The decrease of potential energy should result in the increase of kinetic energy, however, the total dissipation of mechanical energy overweigh the internal energy conversion. The increase of air density during the later stage of the flight causes more severe energy loss thus the decline gradient of velocity enlarges in the meantime.

It depends on the application of the vehicle to judge the trajectory performance. Since the reentry process has plenty of leaps, it brings challenge to flight control. Moreover, a great number of leaps cause a long flight time leading to a large amount of heating flux to the vehicle which challenges the vehicle's material and structure. However, the final landing velocity is 418 m/s, which is low enough for a safe landing. Therefore, this kind of vehicle can be referred to according to different mission.

## Conclusion

This paper introduced a novel design approach of wide-speed-range vehicle based on streamline tracing technique. The aerodynamic configuration of the vehicle generated by this novel method is mainly affected by the upper surface's base curve, which is parameterized in this article. Numerical analysis and trajectory analysis has been applied on a typical vehicle generated by this approach.

The numerical analysis proved that the wide-speed-range vehicles designed in this article have good performance within the design Mach number range. They own good wave-ride performance in the design speed range and their undersurfaces suffer more uniform pressure in a wide speed range than waveriders, which gives them a bright prospect. The aerodynamic properties also show a trade-off between the waveriders designed in the two Mach number sides. The wide-speed-range HGV designed with design Mach number decreasing from the edge to the vehicle's symmetric plane continuously performs better than the vehicle designed with design Mach number increasing from the edge to the vehicle's symmetric plane. Trajectory analysis shows a saltatory ballistic curve with quickly dissipating mechanical energy. The trajectory owns long cross range and low landing velocity, which is meaningful in mission design.

In summary, wide-speed-range HGV is designed to overcome the aerodynamic difficulties traditional gliding vehicle encountered when they travel in a wide speed range. The design approach proposed in this article is worth consulting in aircraft design. However, further effort is needed to validate the performance of the vehicles designed in this approach.

## References

- [1]. Küchemann D. Hypersonic aircraft and their aerodynamic problems [J]. *Progress in Aerospace Sciences*, 1965, 6: 271-353.
- [2]. Ding F, Shen C-b, Liu J et al. Influence of surface pressure distribution of basic flow field on shape and performance of waverider [J]. *Acta Astronautica*, 2015, 108: 62-78.
- [3]. Chen X-q, Hou Z-x, Liu J-x et al. Bluntness impact on performance of waverider [J]. *Computers & Fluids*, 2011, 48(1): 30-43.
- [4]. Liu J-x, Hou Z-x, Chen X-q et al. Experimental and numerical study on the aero-heating characteristics of blunted waverider [J]. *Applied Thermal Engineering*, 2013, 51(1-2): 301-314.
- [5]. Liu J-x, Hou Z-x, Ding G-h et al. Numerical and experimental study on waverider with blunt leading edge [J]. *Computers & Fluids*, 2013, 84: 203-217.
- [6]. Lobbia MA, Suzuki K. Experimental Investigation of a Mach 3.5 Waverider Designed Using Computational Fluid Dynamics [J]. *AIAA Journal*, 2014, 53(6): 1590-1601.
- [7]. Viviani A, Pezzella G. *Aerodynamic and Aerothermodynamic Analysis of Space Mission Vehicles* [M]. Switzerland: Springer International Publishing, 2015.
- [8]. John D. Anderson J. *Fundamentals of Aerodynamics* [M]. McGraw-Hill Education (Asia), 2011.
- [9]. Dalle DJ, Driscoll JF, Torrez SM. Ascent Trajectories of Hypersonic Aircraft: Operability Limits Due to Engine Unstart [J]. *Journal of Aircraft*, 2014, 52(4): 1345-1354.
- [10]. Liu X, Shen Z. Rapid Smooth Entry Trajectory Planning for High Lift/Drag Hypersonic Glide Vehicles [J]. *Journal of Optimization Theory and Applications*, 2016, 168(3): 917-943.

- [11]. Zhao J, Zhou R. Particle swarm optimization applied to hypersonic reentry trajectories [J]. Chinese Journal of Aeronautics, 2015, 28(3): 822-831.
- [12]. Zhao J, Zhou R. Reentry trajectory optimization for hypersonic vehicle satisfying complex constraints [J]. Chinese Journal of Aeronautics, 2013, 26(6): 1544-1553.